Journal of Asian Earth Sciences 298 (2026) 106940

Contents lists available at ScienceDirect

Journal of Asian Earth Sciences

journal homepage: www.elsevier.com/locate/jseaes

Full length article

The rupture process of the September 2022 Guanshan and Chishang Earthquakes: Joint inversion of seismological and geodetic data

Wei-Yu Zhang [a], Yu-Sheng Sun [b], Yopi Serhalawan [a,c,d,*], Po-Fei Chen [a], Ming-Che Hsieh [e], Wu-Lung Chang [a,e]

[a] Department of Earth Sciences, National Central University, Taoyuan, Taiwan, ROC
[b] Department of Earth Sciences, University of Oregon, Eugene, OR 97403, USA
[c] Taiwan International Graduate Program - Earth System Science (TIGP-ESS), Academia Sinica and National Central University, Academia Sinica, Taipei 11529, Taiwan, ROC
[d] The Indonesian Agency for Meteorological, Climatological and Geophysics, Indonesia
[e] Earthquake-Disaster and Risk Evaluation and Management Center (E-DREaM), National Central University, Taoyuan, Taiwan, ROC

ARTICLE INFO

Keywords:
Joint inversion
Rupture process
Guanshan Earthquake
Chishang Earthquake
Coulomb stress
Barrier

ABSTRACT

On 17–18 September 2022, the Mw 6.5 Guanshan and Mw 7.0 Chishang earthquakes, struck the Longitudinal Valley (LV) of Taiwan, the collision boundary between the Eurasian plate and the Philippine Sea plate. Aftershock patterns show that the events occurred within 24 h, only a few kilometers apart, and that both ruptured the west-dipping Central Range Fault (CRF). To investigate their rupture behavior and interaction, we performed a joint inversion of teleseismic, strong-motion, and GNSS data. The resulting finite fault models revealed distinct rupture characteristics, with the Guanshan earthquake mainly rupturing down-dip with minor shallow southward extension, in contrast to the Chishang earthquake, which propagated northward toward the surface and produced two shallow asperities. Combining these models with static Coulomb stress calculations and rupture-velocity analysis indicates that Guanshan may have promoted failure of the Chishang segment through static stress transfer, and that a low-velocity zone and clustered aftershocks between the two hypocenters are consistent with a barrier that limited the northward extent of the Guanshan rupture.

1. Introduction

Taiwan is located at the collision boundary between the Eurasian plate (EUP) and the Philippine Sea plate (PSP), across which the northwesterly convergence rate is approximately 8 cm/yr. According to GPS observations (Yu and Liu, 1989; Yu et al., 1997; Yu and Kuo, 2001), nearly half of the EUP-PSP convergence (3–4 cm/yr) is currently accommodated across the Longitudinal Valley (LV), a 180 km long suture zone trending NNE-SSW in eastern Taiwan, making LV seismically active (Fig. 1).

The active LV is primarily composed of two major seismogenic structures bonding its edge: the east-dipping Longitudinal Valley Fault (LVF) on the eastern flank and the west-dipping Central Range Fault (CRF) on the western flank (e.g., Shyu et al., 2005a, b; Shyu et al., 2006a, b). The high slip rates of LVF are realized either through active seismicity depicting fault geometries (Kuochen et al., 2004) with occasional prominent moment release [e.g., the 1951 series (Cheng et al., 1996; Chen et al., 2008); the 1972 Ruisui earthquake (Kao et al., 1998); the 2003 Chengkung earthquake (Ching et al., 2007; Kuochen et al., 2007); and the 2024 Hualien earthquake (Chien et al., 2025)], or through continuous creeping as observed by creepmeters at the Chishang segment (Lee et al., 2001, 2003). On the other hand, the role of CRF on the suturing process across LV has been obscured seismically in the past few decades – with only far and few in between [e.g., the 2006 Taitung earthquake (Wu et al., 2006); the 2013 Ruisui earthquake (Chuang et al., 2014)]. It is the geomorphic analysis of the uplifted fluvial terraces on the western bank and in the central reached of LV, between just north of the Wuhe Tableland to near Chishang, that supports the involvements of CRF on Taiwan orogeny (Shyu et al., 2006a).

In this tectonically complex and seismically active region, the south-central LV was struck by two large earthquakes within a day. On 17 September 2022 at 13:41:19.11 UTC, a Mw 6.5 earthquake (ML 6.6, as estimated by the Central Weather Administration, Taiwan; CWA) occurred, referred to as the Guanshan earthquake. Less than 24 h later,

* Corresponding author at: Department of Earth Sciences, National Central University, Taoyuan, Taiwan, ROC.
E-mail address: yopi.serhalawan@bmkg.go.id (Y. Serhalawan).

https://doi.org/10.1016/j.jseaes.2025.106940
Received 23 September 2025; Received in revised form 30 November 2025; Accepted 24 December 2025
Available online 25 December 2025

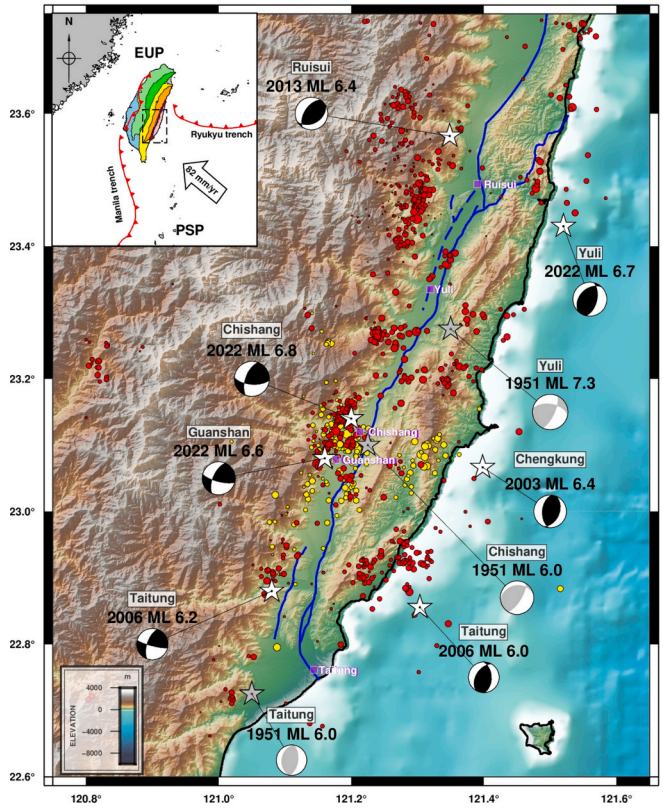

Fig. 1. Tectonic setting of the 2022 Guanshan and Chishang earthquakes. White stars indicate the epicenters of earthquakes with ML > 6 that occurred in the south-central part of the Longitudinal Valley (LV) over the past two decades. Epicenter data are sourced from the Geophysical Database Management System (GDMS) earthquake catalog, and focal mechanisms are from the Global CMT catalog. Gray stars represent three ML > 6 earthquakes that occurred in the south-central part of the LV during the Hualien-Taitung earthquake sequence in 1951 (Chen et al., 2008). The inset displays the study area and its geological structures as classified by the Central Geological Survey (CGS) of Taiwan: from west to east—Coastal Plain (sky blue), Western Foothills (light green), Hsueshan Range (green), West Central Range (yellow), East Central Range (orange), Longitudinal Valley (red), and Coastal Range (pink). Active faults (blue lines) and subduction trenches (red lines) are also shown. (For interpretation of the references to colour in this figure legend, the reader is referred to the web version of this article.)

on 18 September 2022 06:44:15.25 UTC, another Mw 7.0 earthquake (ML 6.8, CWA) occurred, referred to as the Chishang earthquake. These events caused several surface breaks and building collapses, including one casualty. According to CWA's reports and the distribution of aftershocks, two intriguing phenomena were noted. First, these earthquakes exhibited a close spatiotemporal relationship. The time interval of occurrence was less than 24 h, and they were only 7 km apart. Secondly, the aftershock distributions and focal mechanisms imply that both events may have ruptured on the west-dipping CRF, which is relatively less active than the LVF. Thus, the occurrence of these two earthquakes provides a valuable opportunity to investigate the rupture characteristics of CRF in the south-central LV.

To gain a deeper insight into the source characteristics of these two earthquakes, we determined the finite fault models using multiple geophysical datasets, including teleseismic waveforms (P, SH, Rayleigh, Love), strong-motion records, and geodetic data (static and high-rate GNSS data). Subsequently, we conducted an in-depth analysis to examine whether there was a static triggering phenomenon between the Guanshan earthquake and the Chishang earthquake from both static and dynamic perspectives. This analysis involved calculating Coulomb stress changes and evaluating rupture velocity.

2. Data processing and inversion methods

We utilized seismological data (teleseismic and strong-motion), along with static and high-rate GNSS, to model the kinematic rupture processes of the Guanshan earthquake and the Chishang earthquake using a nonlinear inversion method. This section details the data processing and the inversion procedure.

2.1. Data

The kinematic rupture models were established using multiple geophysical datasets. For the Guanshan earthquake, we selected a total of 85 broadband teleseismic waveforms (with epicentral distances ranging from 30° to 90°) that exhibited high signal-to-noise ratios and provided good azimuthal coverage. The data were accessed from the NSF SAGE data archive operated by EarthScope Consortium (NSF award 1724509). These waveforms included 24P-waves, 26 SH-waves, 19 Rayleigh waves and 16 Love waves. The ground displacements were resampled at intervals of 0.2 s for P and SH waves and 4 s for Rayleigh and Love waves. We also selected 42 strong ground motion waveforms within an epicentral distance of ≤ 60 km from the Taiwan Strong Motion Instrumentation Program (TSMIP) network (Liu et al., 1999), maintained by the CWA. The acceleration waveforms were integrated to velocity and underwent basic baseline correction following Wang et al. (2011). In addition, we used 45 static GNSS displacements and 27 high-rate GNSS time series within an epicentral distance of ≤60 km.

Regarding the Chishang earthquake, we selected 108 broadband teleseismic waveforms, including 31 P-waves, 31 SH-waves, 26 Rayleigh waves, and 20 Love waves. Subsequently, the ground displacements were resampled at intervals of 0.2 s for teleseismic body waves and 4-second intervals for teleseismic surface waves. We selected 44 strong ground motion waveforms within an epicentral distance of ≤80 km. The baseline-corrected acceleration waveforms were integrated to velocity. We also used 92 static GNSS displacements and 73 high-rate GNSS time series within an epicentral distance of ≤80 km. The records and locations of the stations used in the inversion for both earthquakes are provided in the Supplement.

The band-pass filter selection criteria were defined separately for teleseismic and regional datasets. For teleseismic body waves, we used an automatic four-corner cosine taper that adapts to centroid time shift and source depth (Goldberg et al., 2022), yielding P and SH band-pass of 0.01–1.0 Hz for Guanshan and 0.006–1.0 Hz for Chishang. Long-period surface waves were limited to 0.004–0.006 Hz, with an outer taper at 0.003 and 0.007 Hz. These choices lie within ranges commonly used in teleseismic finite-fault inversions (e.g., Shao et al., 2011; Sianipar et al., 2022; Yan et al., 2022; Chien et al., 2025). For regional datasets (TSMIP strong-motion and high-rate GNSS), the frequency range was determined from frequency-domain coherence between observations and Green's-function synthetics (Melgar & Bock, 2015). Accordingly, strong-motion data were band-passed 0.02–0.125 Hz for Guanshan and 0.01–0.3 Hz for Chishang, and high-rate GNSS time series were low-pass filtered at 0.125 Hz and 0.3 Hz, respectively. All regional records were sampled at 0.2 s.

2.2. Faulting geometry

Lee et al. (2006) demonstrated that imprecise faulting geometries can lead to artificial slip distributions, particularly when static GNSS data are used in inversion. To reduce this effect, we adopted an optimal fault geometry strategy by individually inverting static GNSS data using a grid search approach. In each iteration, the strike and dip were varied in 1° increments over a ± 20° range around the west-dipping nodal planes of the Global Centroid Moment Tensor (CMT) solution (Ekström et al., 2012), which served as the initial reference for both earthquakes. All other inversion settings and parameters were kept identical to those used in the final finite-fault models. For each trial plane, we calculated a

normalized misfit between the observed and modeled static GNSS displacements, and the plane with the smallest misfit was selected as the preferred geometry. The uncertainty in strike and dip was then assessed from the misfit distribution by identifying all models with normalized misfits within 10 % of this minimum value; for both earthquakes, these acceptable models form a compact cluster around the preferred strike and dip, indicating that the fault orientations are well constrained (Fig. 2).

For the Guanshan earthquake, the grid search converged on a strike of 206° and a dip of 55°, while for the Chishang earthquake, the result differed by only 1° in dip relative to the Global CMT solution; accordingly, the Global CMT strike and dip parameters were adopted (Fig. 2). We initially followed the fault dimension strategy of Goldberg et al. (2022) to define physically reasonable fault dimensions. The fault length was estimated based on the centroid time delay and assumed rupture velocity, while the width was constrained by the dip angle and hypocentral depth to ensure the fault plane remained within the expected seismogenic thickness. Both parameters were then adjusted using the aftershock distribution and the slip pattern resolved from the inversion. The correspondingfault model for the Guanshan earthquake was defined with a length of 42 km and a width of 27 km, discretized into subfaults measuring 3 km by 3 km. For the Chishang earthquake, the model dimensions were 90 km in length and 28.8 km in width, with subfaults of 3 km by 3.6 km. Finally, the CWA hypocenters were used as the nucleation points for both events.

2.3. Inversion strategy

We performed a joint inversion using the Wavelet and Simulated Annealing SliP (WASP) package, an extension of Koch et al. (2019). This approach incorporates multiple datasets: teleseismic broadband, regional accelerometer, high-rate and static GNSS, and InSAR data (Goldberg et al., 2022). This inversion scheme relies on the nonlinear heat-bath simulated annealing algorithm and solves for optimal solutions of slip amplitude, rake angle, initial rupture time, and rise time on each subfault in the wavelet domain (Ji et al., 2002). For each parameter, we defined distinct search bounds following the methodology of Goldberg et al. (2022). For these shallow crustal events, we adopt a reference rupture velocity of 2.5 km/s (Koch et al., 2019; Goldberg et al., 2022) and constrain rupture initiation times so that the implied rupture velocity lies within a physically reasonable range of roughly 1.0–3.125 km/s along the fault. After the inversion, we estimate the rupture velocity at each subfault as the on-fault distance from the hypocenter divided by the inverted rupture initiation time (e.g., Shao et al., 2011).

Green's functions for each subfault were computed using the 1D Taiwan average crust velocity model (Chen and Shin, 1998). Specifically, teleseismic body-wave Green's functions were calculated according to Yao and Ji (1997), while those for teleseismic surface waves were derived via normal mode summation (Shao et al., 2011). For regional data (including strong-motion accelerometer records and both static and high-rate GNSS observations), the Green's functions were generated using a frequency-wavenumber integration method (Zhu and Rivera, 2002).

Based on the logical weighting scheme proposed by Goldberg et al. (2022) for various types of observations, the assigned weights to the datasets are outlined as follows: for the teleseismic waveforms, P-waves were given twice the weight of SH-waves due to their higher signal-to-noise ratios and lower arrival-time uncertainty. Surface waves received quadruple the weight of SH-waves, reflecting the higher reliability of their long-period Green's functions compared to body waves (Shao et al., 2011). Regarding the near-field observations, the strong motion waveforms and the horizontal components of high-rate GNSS were weighted equivalently to teleseismic surface waves, while the vertical components of both static and high-rate GNSS data were assigned half the weight of their horizontal components, due to their lower accuracy (Bock et al., 2011; Melgar et al., 2017, 2020). Furthermore, to account for the greater sensitivity of near-fault recordings to rupture details, stations in closest proximity to the fault were assigned double weight (Liu et al., 2019).

2.4. Coulomb stress change

The Coulomb stress change quantifies the adjustments of normal and shear stress on the fault and is widely applied to examine static stress triggering (Goldberg et al., 2020; Li et al., 2020; Wang et al., 2020). In this study, we calculated the Coulomb stress change induced by the Guanshan earthquake, using an open-source code developed by Materna (2023). Based on the elastic dislocation theory (Okada, 1985), this code calculates displacements, strains, stresses, and Coulomb stress changes in a homogeneous elastic half-space. A friction coefficient of 0.4 was assumed, consistent with previous studies (Freed, 2005; Goldberg et al., 2020; Wang et al., 2020).

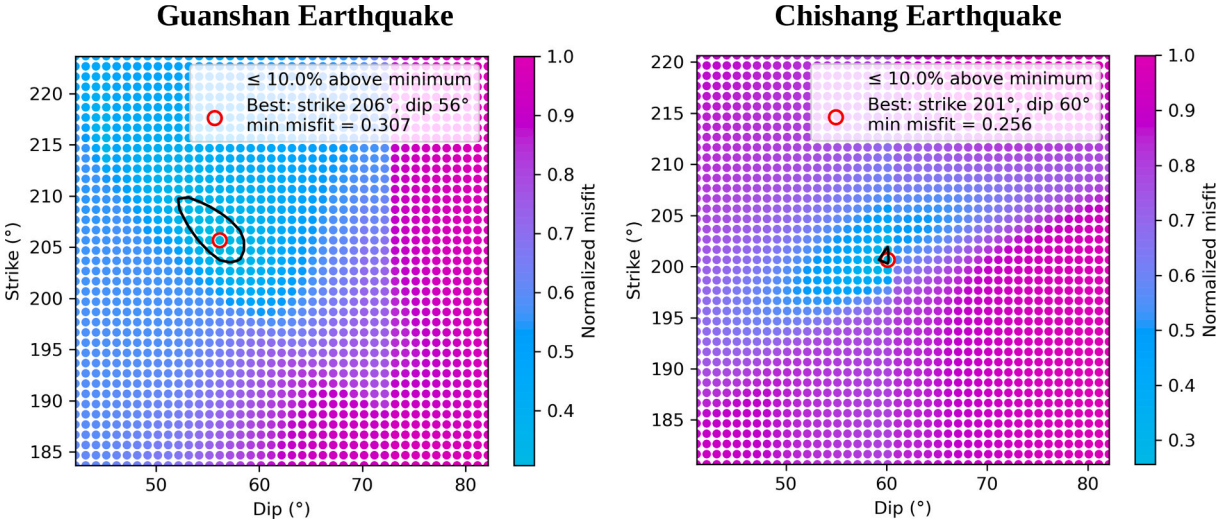

Fig. 2. Results of the fault-geometry grid search for the Guanshan (left) and Chishang (right) earthquakes, derived from the inversions of static GNSS data. The color scale represents the normalized misfit, with light blue indicating a better fit. Red circles denote the best-fit strike and dip, obtained by systematically varying each parameter at 1° intervals within a ± 20° range relative to the west-dipping Global CMT nodal plane. Black contours denote the ≤ 10 % misfit region, which defines the strike–dip uncertainty. (For interpretation of the references to colour in this figure legend, the reader is referred to the web version of this article.)

3. Inversion results

3.1. The Guanshan earthquake

The primary rupture of the Guanshan earthquake is concentrated around the hypocenter and exhibits a southward propagation trend (Figs. 3a, b). The estimated moment magnitude for this event is Mw 6.6 (1.59×10^{18} Nm). The average inverted rake angle is approximately 25°, indicating predominantly left-lateral faulting motion across an overall rupture area of ~430 km^2. Two distinct asperities are identified on the rupture plane. The principal slip area (Asperity I) is situated around the hypocenter, covering an approximate area of 18 × 15 km^2. Upon closer examination, Asperity I can be further divided into two subdivisions, with the lower subdivision being dominant, with a peak slip around 1.4

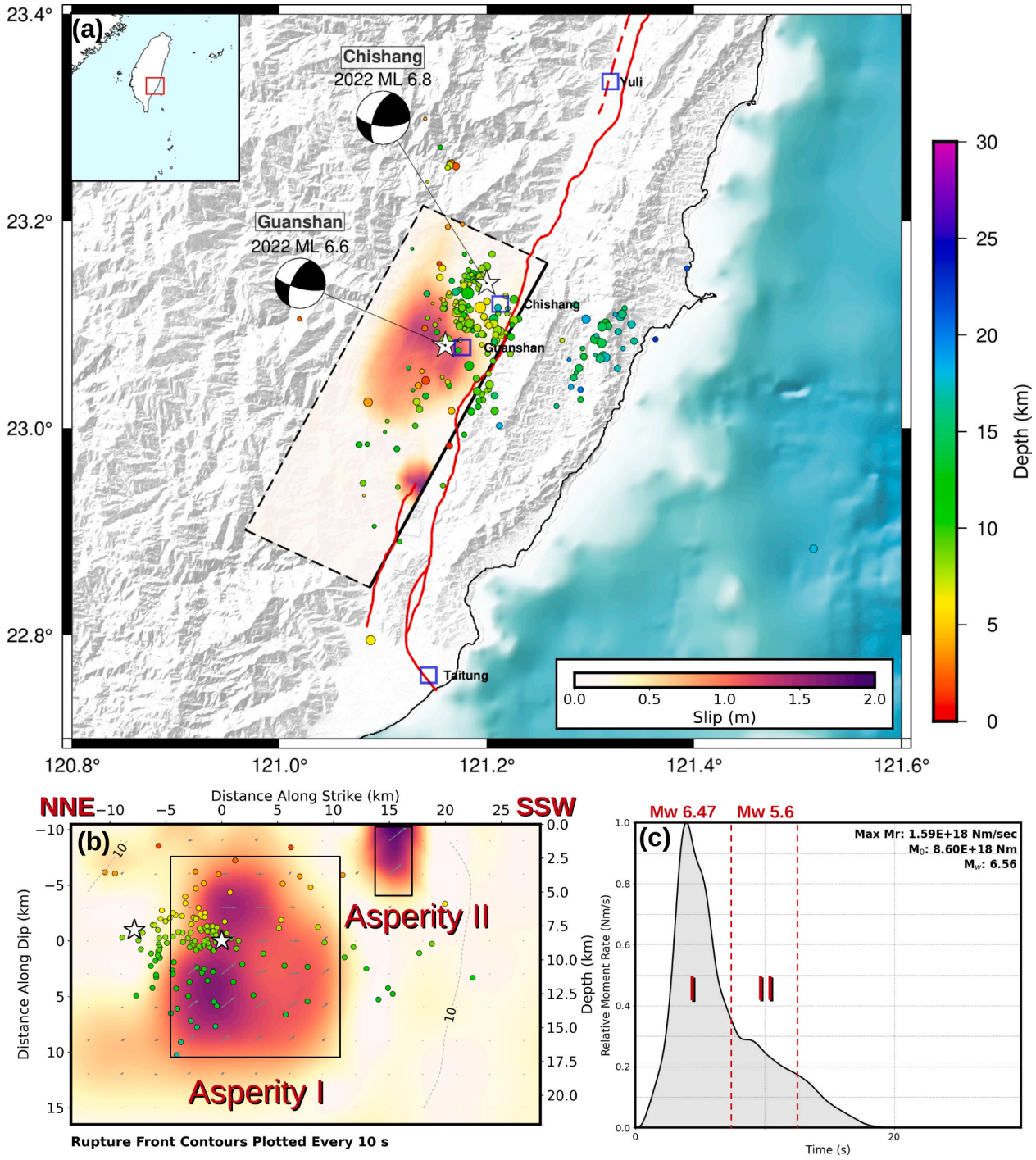

Fig. 3. Finite fault model for the Guanshan earthquake. (a) Slip distribution projected vertically onto the surface. White stars represent the epicenters of the Guanshan earthquake and the Chishang earthquake; circular dots represent earthquakes in the GDMS catalog that occurred between the Guanshan earthquake and the Chishang earthquake (UTC time from 2022/09/17 13:42:28 to 2022/09/18 06:35:41). Red solid and dashed lines represent active faults published by the CGS; black solid lines denote the shallowest boundaries of the fault model. (b) Slip distribution on the fault plane. The black rectangle represents the main slip area, with colors indicating the magnitude of slip; gray dashed lines depict contour lines of the rupture front, spaced at 10 s. (c) Moment-rate function. (For interpretation of the references to colour in this figure legend, the reader is referred to the web version of this article.)

m and exhibiting more thrust components. Asperity II is located to the south of the hypocenter, covering an area of 6 × 3 km^2; it extends to the surface, exhibits a maximum slip of 1.85 m, and involves both thrust and strike-slip motion. To understand the spatial relationship between aftershock distribution and slip, we projected the earthquake events that occurred between the origin time of the Guanshan earthquake and the Chishang earthquake (17 September 2022, 13:42:28 UTC to 18 September 2022, 06:35:41) (Figs. 3a, b). The events are predominantly clustered in the vicinity of the primary slip area, with a discernible concentration between the northeastern edge of Asperity I and the hypocenter of the Chishang earthquake.

Temporal analysis shows that during the first 3 s following the initiation of rupture, the slip propagated primarily in the dip direction (Fig. 4). Subsequently, the rupture advanced southward and upward toward the shallow portion of the fault, culminating in the formation of Asperity I around 9 s after initiation. Concurrently, Asperity II starts to slip and approximately completes its rupture by the 14 s. The inversion yields an average rupture velocity of 2.26 km/s, corresponding to 75 % of the local S-wave velocity, which falls within the typical range observed in seismic source studies (65–85 % of S-wave velocity; Heaton, 1990). Analysis of the reference rupture front, defined by the average rupture velocity, together with the progression of slip, reveals that the shallow area above the source region exhibits significant slip only 2–3 s after the rupture front has passed. This observation implies a comparatively slower rupture velocity in this region.

The moment-rate function (MRF) of the Guanshan earthquake exhibits a single, triangular peak in seismic moment release (Fig. 3c). This triangular moment-rate function is similar to the shape of far-field P-waves, as observed at stations such as COLA and KDAK (Figs. S1 and S5). The maximum seismic moment rate occurs within 3 to 4 s after the rupture initiation, corresponding to the rupture of Asperity I.

3.2. *The Chishang earthquake*

Fig. 5 shows the slip distribution and MRF derived from the joint inversion for the Chishang earthquake. The inverted fault model reveals

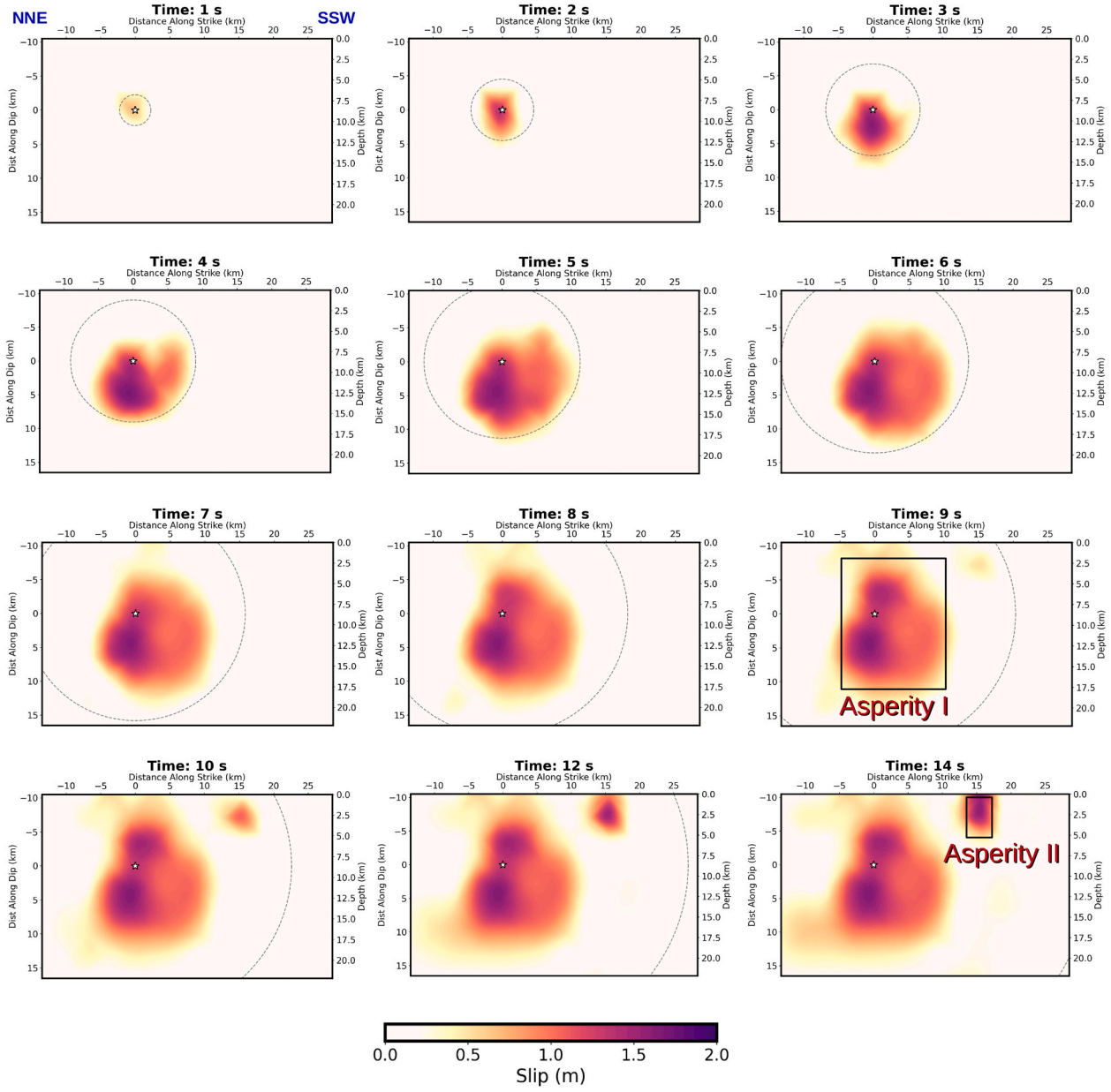

Fig. 4. Snapshots of the cumulative slip distribution for the Guanshan earthquake at 1 s intervals. The dashed gray line represents the reference rupture front with an average rupture velocity of 2.26 km/s.

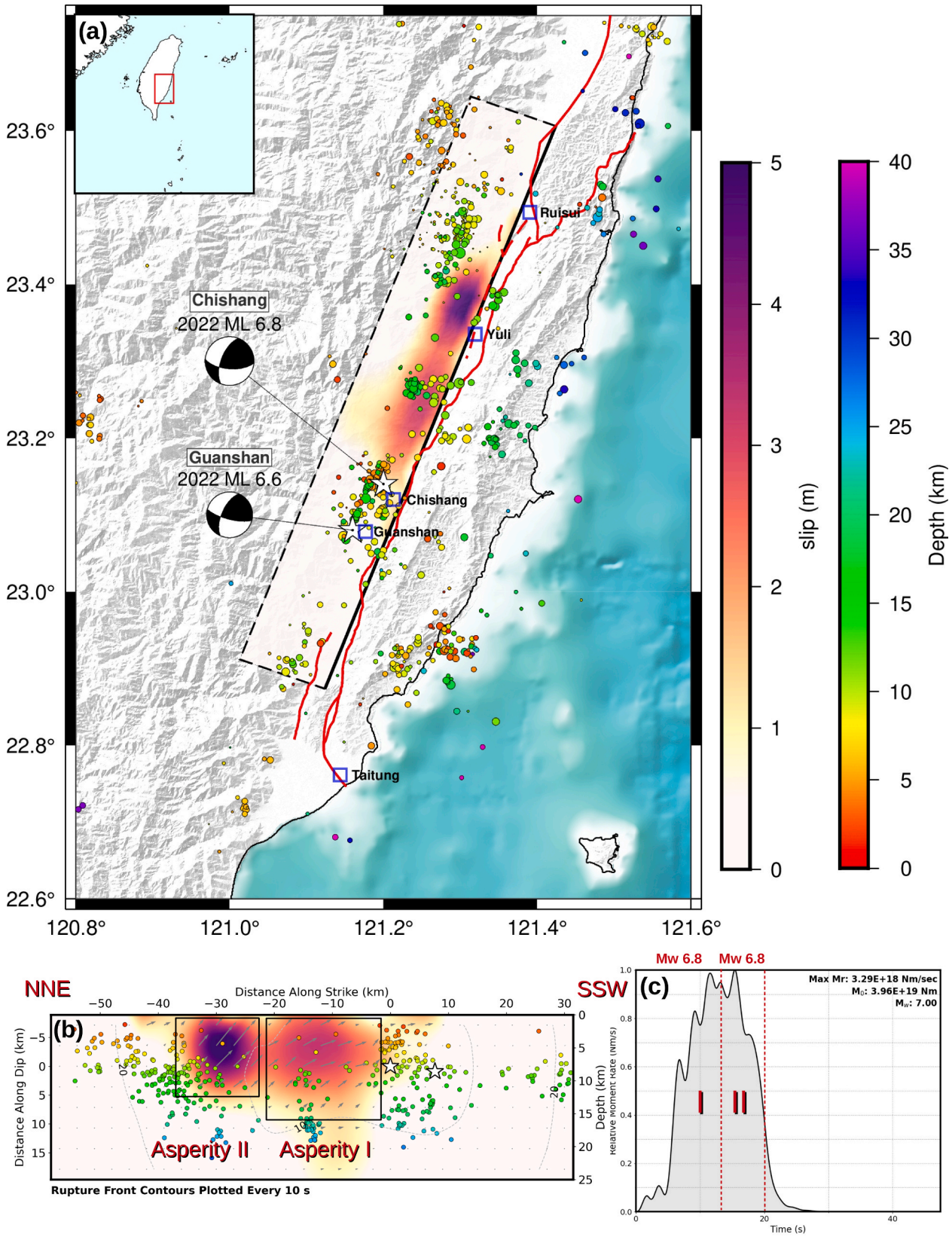

Fig. 5. Same as Fig. 3 but for the Chishang earthquake, including one month of its aftershocks.

that the primary slip distribution is concentrated north of the hypocenter, with an average rake angle of ~33° over an overall rupture area of approximately 750 km^2. The slip pattern indicates two distinct asperities in the shallow part, each releasing a comparable seismic moment corresponding to Mw 6.8. The first slip area (Asperity I), located closer to the hypocenter, extends primarily from the near surface to a depth of 15 km, with slip propagating in the dip direction to reach a depth of 25 km. This asperity covers an area of approximately 21 × 14.4

km^2 and is characterized by predominantly left-lateral motion with a reverse component, exhibiting a maximum slip of about 3.2 m. In contrast, the second slip area (Asperity II) is situated ~30 km north of the epicenter, near Yuli Township, Hualien County. Compared with Asperity I, Asperity II is more compact, has a larger reverse component, covers an area of approximately 9 × 10.8 km^2 and reaches a maximum slip of 5.0 m. Projection of aftershocks occurring within one month following the Chishang earthquake shows that these events mainly occur at the edges of the asperities, consistent with previous studies that aftershocks tend to cluster around asperity regions (Das and Henry, 2003; Lee et al., 2014; Wetzler et al., 2018; Sun et al., 2024).

Fig. 6 shows the complex rupture process of the Chishang earthquake. Initially, the rupture propagated northward with an average rupture velocity of 2.0 km/s, equivalent to 66 % of the S-wave velocity in the source area. Comparing the average rupture velocity (the preset rupture front) with the subsequent slip development, we found that within the first 5 s after rupture onset, the effective rupture velocity was reduced to 1.0–1.5 km/s, corresponding to a slower development of slip.

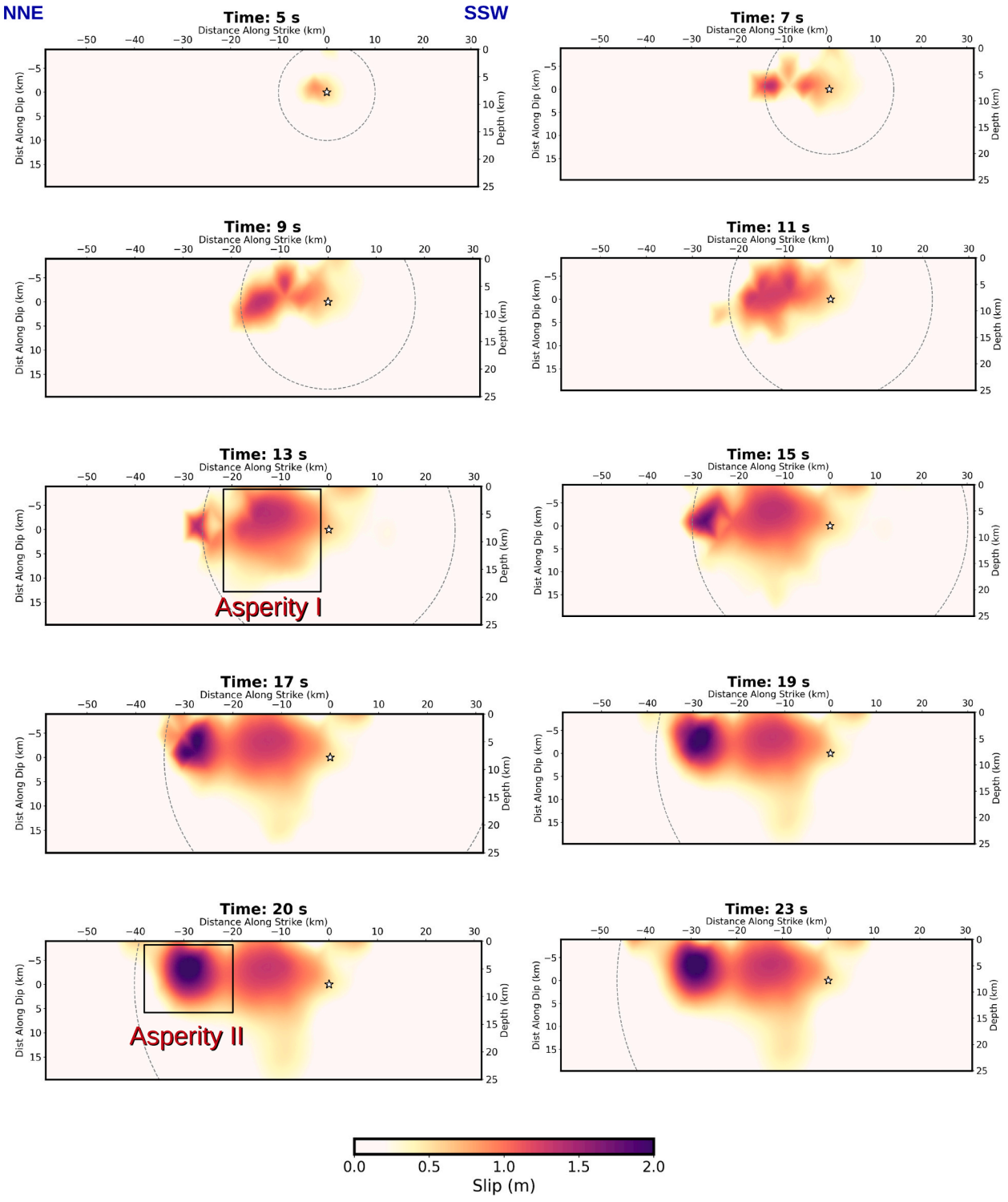

Fig. 6. Same as Fig. 4 but for the Chishang earthquake. The dashed gray line represents the reference rupture front with an average rupture velocity of 2.01 km/s.

Although the maximum accumulated slip in this interval is close to 2 m, the initial seismic moment release remains relatively low due to the slower expansion of the rupture area (Fig. 5c). After the first 5 s, the rupture accelerates, leading to significant slips and the formation of Asperity I around 13 s. Concurrently, Asperity II begins to rupture and expand northward until ~20 s, and as it develops, Asperity I appears to extend further in the dip direction.

The MRF of the Chishang earthquake reflects its complex rupture dynamics. During the first 5 s, the event releases a relatively small amount of seismic moment, corresponding to Mw 6. Following this initial phase, as both asperities develop, the seismic moment is released more significantly. In particular, during the rupture of Asperity I, the MRF displays at least three distinct peaks at approximately 7, 9, and 12 s. The maximum moment rate occurs between 15 and 16 s, which is attributed to the rupture of Asperity II. These temporal features of the moment release can also be inferred from the characteristics of far-field body waves; for example, records from the POHA station reveal an initially weak P-wave amplitude followed by a significant increase in amplitude (Figs. S11 and S15).

4. Discussion

4.1. The advantages of joint inversion

Joint inversion of teleseismic and regional data to determine finite fault models has become a well-established method for studying the kinematic characteristics of earthquakes (Hartzell and Heaton, 1983; Wald et al., 1996; Ji et al., 2002; Lee et al., 2014; Yan et al., 2022). Hartzell and Heaton (1983) emphasized that integrating multiple seismic datasets enhances the analysis of fault rupture processes. Teleseismic data primarily constrain the overall rupture characteristics, whereas strong-motion data provide finer resolution of rupture details.

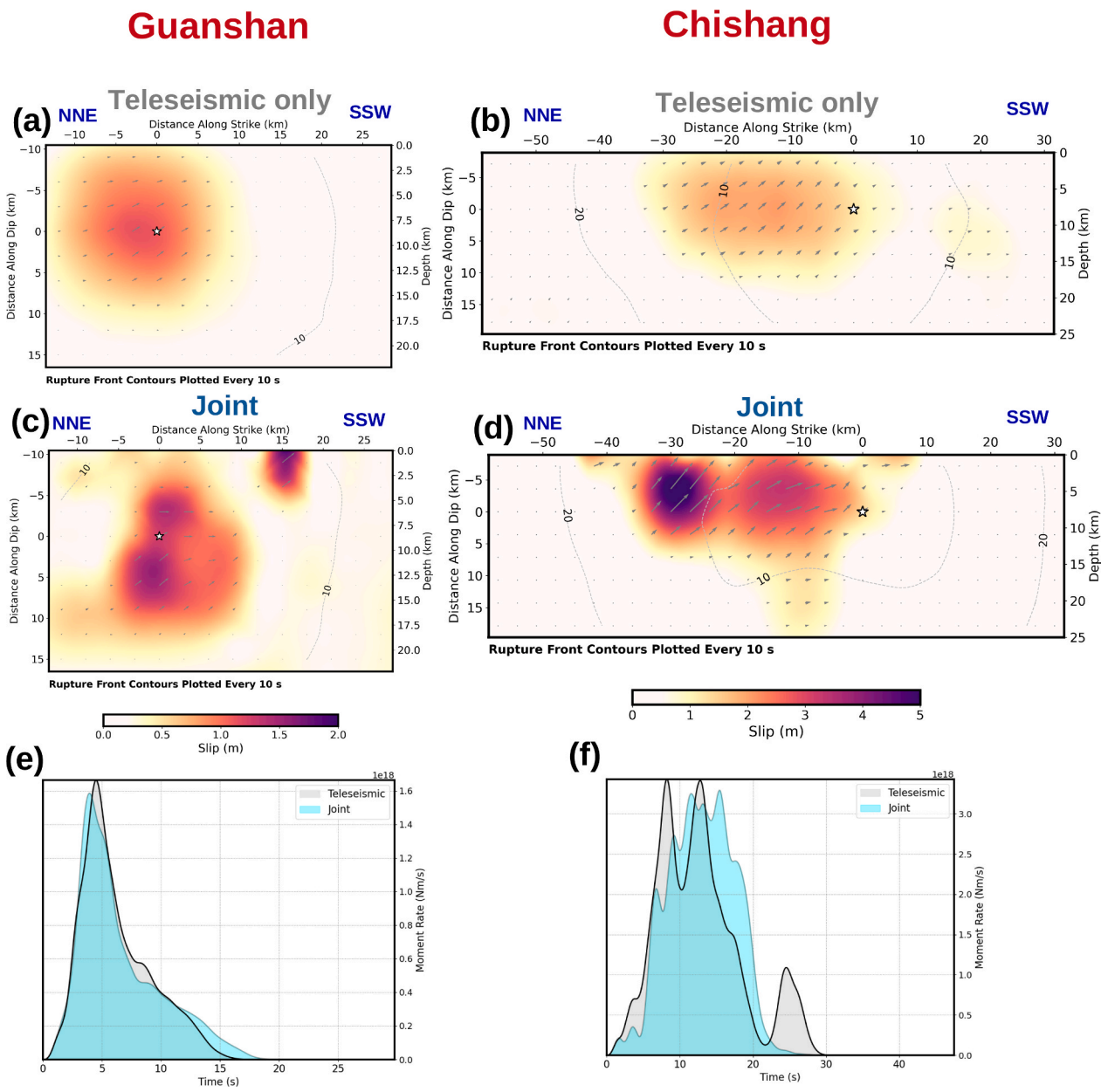

Fig. 7. Comparison of teleseismic and joint inversion models for the Guanshan and Chishang earthquakes. Panels (a) and (b) show the teleseismic inversion models for the Guanshan and Chishang earthquakes, respectively. Panels (c) and (d) present the corresponding joint inversion models. Panels (e) and (f) display the MRFs for the teleseismic (gray) and joint (cyan) inversion models for the Guanshan and Chishang earthquakes, respectively. (For interpretation of the references to colour in this figure legend, the reader is referred to the web version of this article.)

Wald et al. (1996) further demonstrated that integrating seismic and geodetic data in joint inversions improves constraints on the spatio-temporal evolution of slip. incorporating geodetic observations supplies more accurate spatial constraints, enabling the inversion to determine rupture timing more effectively during waveform fitting. As a result, the derived fault model attains higher resolution in both slip distribution and rupture timing.

To examine the contribution of regional data (strong-motion and geodetic observations) to the rupture process modeling, we compared the finite fault models obtained from teleseismic inversion with those obtained from joint inversion for both Guanshan and Chishang earthquakes (Fig. 7). Although the teleseismic inversion yields smoother slip distributions, it generally captures the overall spatial pattern of slip; for instance, both models for the Chishang earthquake exhibit a pronounced northward concentration of slip relative to the hypocenter. In contrast, incorporating regional data produces more heterogeneous slip distributions, resulting in increased seismic moments and higher maximum slip values (Table 1). Specifically, For the Guanshan earthquake, the maximum slip increased from 1.1 m to 1.9 m, and for the Chishang earthquake, it increased from 2.1 m to 5.0 m. These changes indicate an improvement in the spatial resolution due to the inclusion of regional data. In comparing the MRFs (Figs. 7e and 7f), the results show a high degree of similarity between the teleseismic and joint inversion models for both earthquakes, with the Guanshan earthquake showing the closest resemblance. This consistency suggests that while the teleseismic inversion model may have limited resolution in capturing rupture details, it provides a comprehensive analysis of the process of seismic moment release. This finding aligns with the perspective proposed by Goldberg et al. (2022).

To further comprehend the contribution of each dataset to the inversion results, we compared the individual inverted results (Figs. 8, 9). For the Guanshan earthquake, the slip distributions derived from different datasets exhibit notable variations in detail, suggesting that each data type captures distinct aspects of the rupture process. Nevertheless, all datasets (both teleseismic and regional) consistently indicate similar source characteristics, such as comparable rake angles. Notably, while all models display the presence of Asperity I, the teleseismic inversion tends to position it further north and nearer the surface, whereas Asperity II, as shown in the joint inversion, is primarily constrained by the static GNSS data.

For the Chishang earthquake, individual inversion results consistently reveal a northward rupture and a concentration of slip near the surface, underscoring the reliability of the inferred rupture characteristics. Although the inversion results vary slightly among datasets, most individual inversions show two asperities, except for the teleseismic result, which appears relatively smoother. In particular, the Asperity II of the high-rate GNSS dataset is more concentrated toward the north and extends to a deeper area. Although the joint result also indicates a downward extension of the rupture, the high-rate GNSS result shows a slightly more northward location.

In terms of slip distribution, we note that among all individual datasets, static GNSS data is the most similar to the joint inversion result, especially for the Chishang case. This indicates that the static GNSS data play an important role in constraining the total slip distribution in the joint inversion process. Previous studies have similarly highlighted this importance: Lee et al. (2023) noted that static GNSS data predominantly controlled the slip distribution in the Chishang earthquake's joint inversion, and Wald and Heaton (1994) emphasized the role of static GNSS data in constraining the slip distribution of the 1992 Landers earthquake. These findings suggest that static GNSS and waveform data provide complementary constraints on rupture processes. Specifically, static GNSS data resolve spatial slip distribution, while waveform data address rupture timing. Incorporating static GNSS data mitigates the trade-off between spatial location and rupture timing inherent in waveform-only inversions. Static GNSS data establish a foundational slip distribution that is then refined by fitting waveform data to determine optimal rupture timing. This integration resolves ambiguities and enhances the resolution of rupture details. In conclusion, combining static and waveform data in joint inversion significantly improves the resolution of rupture characteristics for both the Guanshan and Chishang earthquakes.

Table 1
Comparison of teleseismic and joint inversion.

Earthquake	Dataset	Moment (Nm)	Peak slip (m)
Guanshan	teleseismic	8.48×10^{18}	1.11
	all*	8.60×10^{18}	1.85
Chishang	teleseismic	3.84×10^{19}	2.05
	all*	3.96×10^{19}	4.99

* teleseismic, strong motion, and static and high-rate GNSS data.

In addition to our internal comparison between teleseismic-only and joint inversions, we also compare our models with recently published InSAR-constrained solutions. He et al. (2024) jointly inverted ALOS-2 InSAR, GPS, strong-motion, and teleseismic data for the same earthquake sequence. For the Guanshan (foreshock) event, both studies retrieve an ~Mw 6.6 momen magnitude with a compact rupture area centered near the hypocenter on the Central Range Fault and predominantly left-lateral oblique-thrust motion. Their distributed-slip model images a single main asperity between ~2 and 14 km depth that does not reach the surface, whereas our joint inversion resolves an additional small shallow asperity that extends to the surface south of the hypocenter. For the Chishang (mainshock) event, both models consistently show a predominantly northward rupture on the Central Range Fault, shallow asperities, and a total seismic moment consistent with Mw 7.0. Our joint model, however, yields somewhat larger peak shallow slip (up to ~5 m compared with ~4 m in He et al., 2024) and a deeper down-dip extension of the southern asperity. These differences in shallow slip amplitude and depth extent probably reflect a combination of factors, including the different data sets used, fault parameterization and model domain, and the choices of regularization and relative data weighting. Nevertheless, the broad agreement in overall moment, rupture extent, and the presence of multiple shallow asperities indicates that the first-order source characteristics are robust across these independent InSAR-constrained and non-InSAR joint inversions.

4.2. Resolution test

To further assess the resolving power and robustness of the joint inversion, we performed synthetic resolution tests for both earthquakes. For each event, we constructed a simplified two-asperity slip model using the same fault geometry and subfault discretization as our final joint-inversion model. The asperity locations and sizes follow the two main slip patches in the joint-inversion result, and each asperity is assigned a single slip amplitude, rake, and rise time that represent the average properties of that patch, while the rupture time on each subfault is kept identical to the kinematic model (Figs. 10 and 11). Synthetic teleseismic, strong-motion, static GNSS, and high-rate GNSS data were then generated using the same station distribution, frequency bands, and Green's functions as in the real-data inversions. These synthetic data were treated as observations and inverted with the same joint inversion setup. We quantify how well the input slip pattern is recovered using a slip-recovery factor R, defined as: $R = 1 - \frac{\sum_i |S_i^{input} - S_i^{inv}|}{\sum_i S_i^{input}} \times 100\%$, where S_i^{input} and S_i^{inv} denote the input and inverted slip on the subfault i, respectively.

For the Guanshan earthquake (Fig. 10), the simplified model consists of a larger asperity (Asperity I) of approximately 18 × 15 km with 1.4 m of slip and a rake of about 25°, and a smaller asperity (Asperity II) of about 6 × 3 km with 1.85 m of slip and a more thrust-dominated rake. The joint inversion of the synthetic data successfully reproduces the

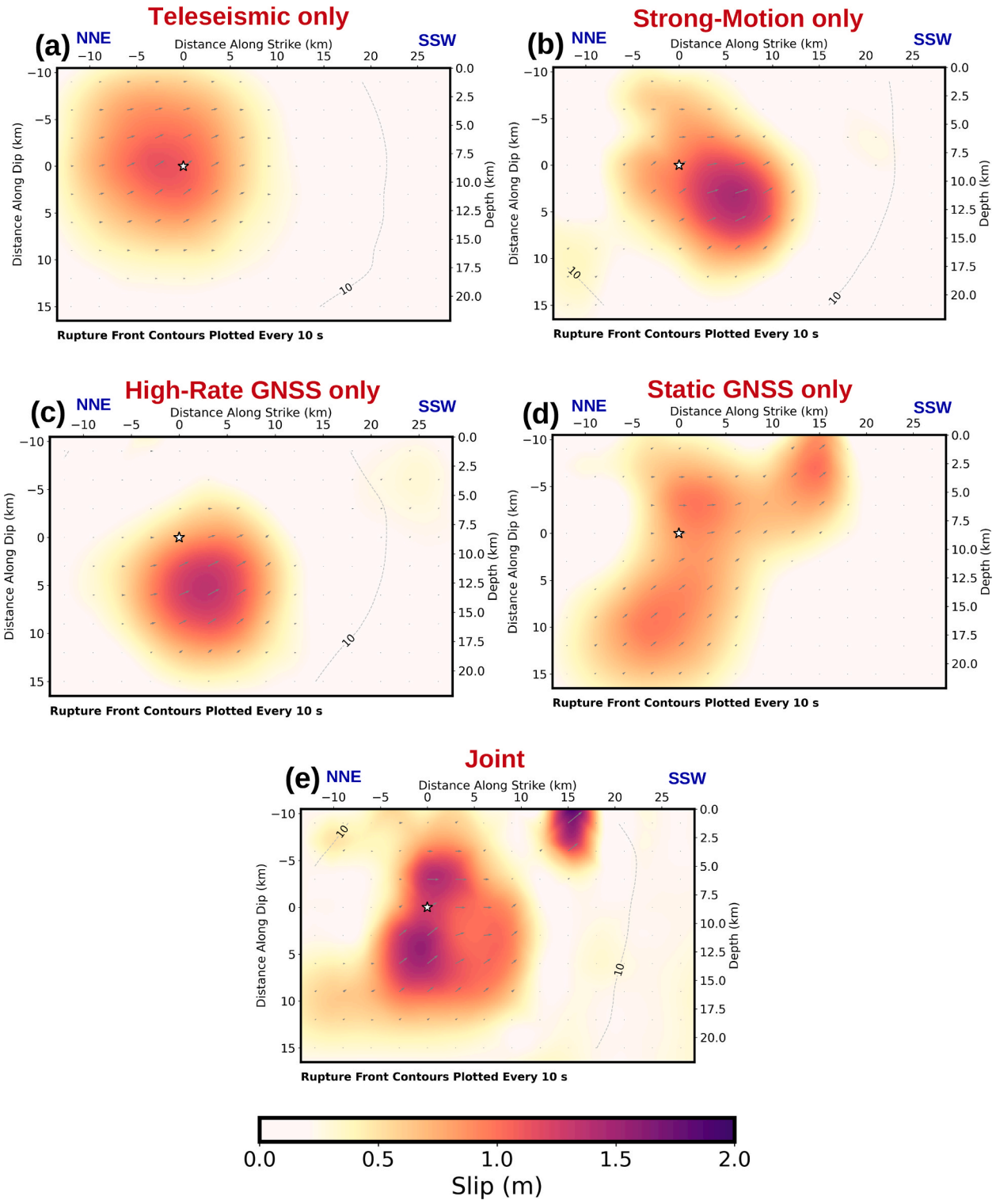

Fig. 8. Individual inversion models for the Guanshan earthquake: (a) teleseismic inversion model, (b) strong-motion inversion model, (c) high-rate GNSS inversion model, (d) static GNSS inversion model, (e) Joint inversion model.

presence and approximate locations of both asperities, indicating that the overall pattern of a compact main patch accompanied by a smaller southern patch is resolvable. However, the recovered slip amplitudes and detailed shapes are less accurate. In the noise-free test, the overall slip-recovery factor is 57 %, and it decreases to 54 % and 48 % when 15 % and 30 % Gaussian noise are added to the synthetic waveforms, respectively. With increasing noise, slip tends to spread beyond the original asperities and their boundaries become more diffuse, although the two-asperity character of the model remains recognizable. These results indicate that, for the Guanshan event, the joint inversion robustly captures the first-order rupture pattern and the relative importance of the two asperities, whereas quantitative estimates of absolute slip are more weakly constrained.

In contrast, the Chishang earthquake (Fig. 11) exhibits markedly better slip resolution in the same type of tests. The simplified model comprises a southern asperity (Asperity I) of about 21 × 14.4 km with

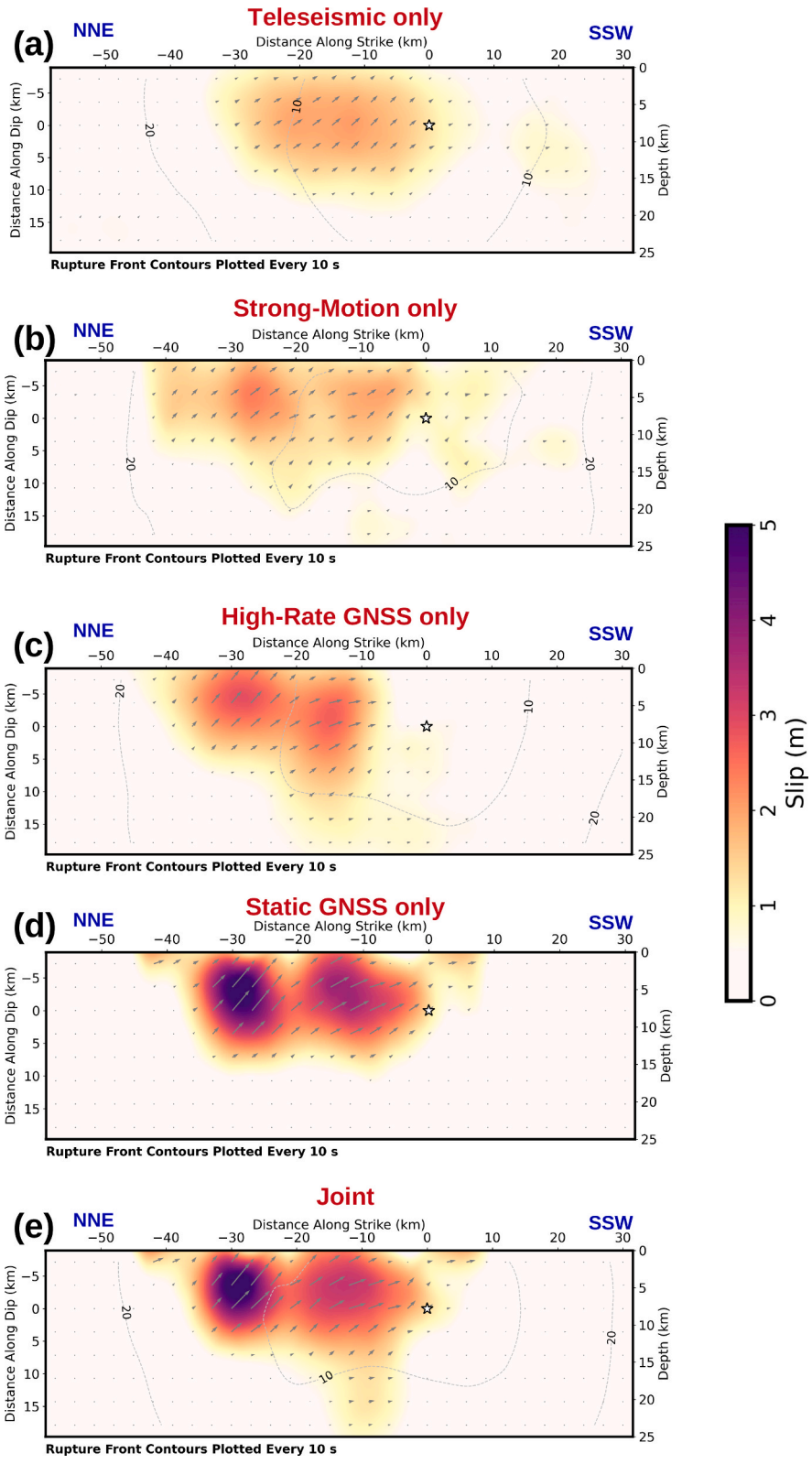

Fig. 9. Same as Fig. 8 but for the Chishang earthquake.

3.2 m of slip and a rake of ~ 30°, extending from the surface down to ~15 km, and a northern shallow asperity (Asperity II) of about 9 × 10.8 km with 5.0 m of slip and a more reverse-dominated rake near Yuli. When the corresponding synthetic multi-data set is inverted, the joint inversion recovers both asperities at nearly the correct locations and with similar shapes. The total slip-recovery factor reaches 68 % in the noise-free case and remains at 67 % and 62 % when 15 % and 30 % Gaussian noise are added, respectively, with the peak slip of the shallow northern asperity reproduced to within only a few percent of the input value. These results demonstrate that, for the Chishang earthquake, the joint inversion provides robust constraints on both the geometry and relative amplitudes of the shallow asperities.

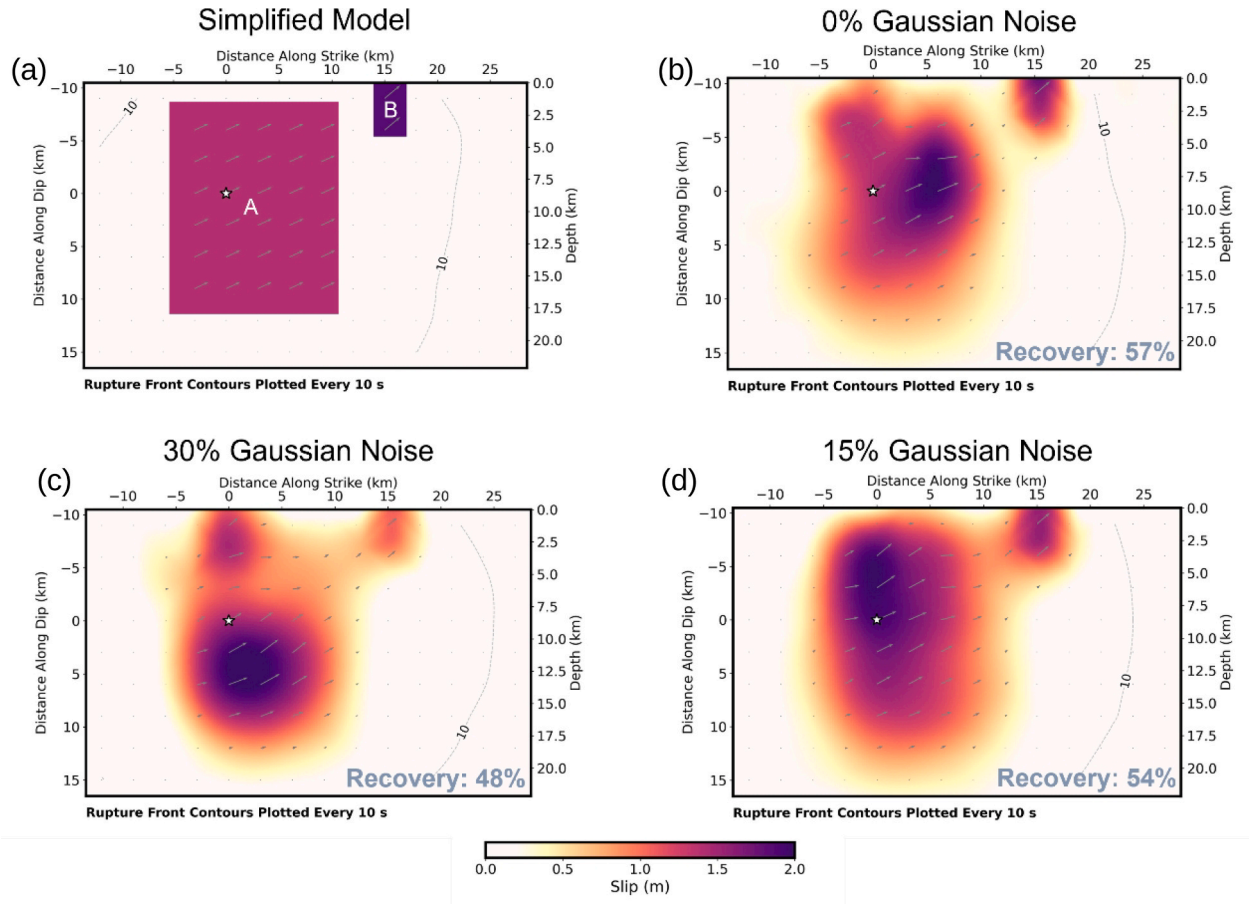

Fig. 10. Synthetic resolution tests for the Guanshan earthquake. (a) Simplified two-asperity input slip model. (b) Inverted slip distribution for synthetic data without added Gaussian noise. (c) Same as (b) but with 15% Gaussian noise added. (d) Same as (b) but with 30% Gaussian noise added. Numbers in the lower-right corner of each panel denote the slip-recovery factor R (in %), which measures how well the input slip distribution is recovered.

4.3. Static stress triggering

The Guanshan and Chishang earthquakes exhibit a close spatiotemporal relationship; both occurred within 24 h, and their epicenters are only 7 km apart. This proximity raises the question of whether a triggering phenomenon exists between these two earthquake events. An earthquake can be considered a process of releasing accumulated regional tectonic stress, which would also adjust the regional stress distribution. This stress adjustment may trigger another earthquake on a different fault (Goldberg et al., 2020; Li et al., 2020; Wang et al., 2020). A fault can be triggered to rupture when normal stress is reduced or shear stress is increased (King et al., 1994; Freed, 2005). To investigate this potential triggering mechanism, we calculated the static Coulomb stress change (ΔCFS) induced by the Guanshan earthquake, resolving it on the Chishang mainshock rupture plane, which we adopt as the receiver fault geometry as our preferred finite-fault model. The results (Fig. 12) indicate that the hypocenter of the Chishang earthquake is situated in a region of positive ΔCFS, characterized by a significant increase in shear stress and a slight positive change in normal stress. The stress state of the region adjacent to the hypocenter is significantly perturbed by the Guanshan earthquake, which could trigger the Chishang earthquake. Additionally, the slip distribution of the Chishang earthquake overlaps well with the region of positive ΔCFS, indicating a strong potential correlation between the two events. This finding is consistent with previous studies. For instance, Lee et al. (2023) similarly identified the hypocenter of the Chishang earthquake as being located in a region of positive Coulomb stress change. They further suggested that the slip distribution appeared to be influenced by the positive ΔCFS induced by the strong foreshock, the Guanshan earthquake.

To assess the sensitivity of these results, we recomputed the ΔCFS for the friction coefficient (μ) between 0.20 and 0.60 in steps of 0.05. For this range of μ, the fraction of receiver patches with positive ΔCFS varies only slightly between 81.3 % and 82.5 %, and 191 out of 240 patches (~80 %) experience positive ΔCFS for all tested μ values, whereas only 13 patches (~5%) change sign and 36 patches (~15 %) remain consistently negative. The overall pattern of positive and negative ΔCFS lobes on the Chishang rupture plane, therefore, changes very little with μ, and the ΔCFS at the Chishang hypocenter is positive for every tested value between 0.20 and 0.60 (Fig. 12d-f). These results demonstrate that our inference that the Guanshan earthquake statistically promoted failure on the Chishang rupture is robust to reasonable uncertainty in μ.

4.4. Implications of seismic dynamics

The aftershock distributions of both earthquakes and the seismogenic structure in the LV strongly suggest that the events occurred along the CRF. This raises an intriguing question: why did two nearby earthquakes, occurring on the same fault, rupture independently? Based on our finite-fault inversion results, we infer that the independence of these events may be due to the presence of a barrier between the hypocenters of the Guanshan and Chishang earthquakes. A barrier is defined as a region on the fault plane that resists rupture propagation due to higher frictional resistance or structural heterogeneity, requiring greater energy to overcome (Yuan et al., 2020). Such barriers are often associated with low rupture velocity, which reflects a higher friction coefficient and greater fracture energy demands during rupture propagation (Zhou et al., 2019; Convertito et al., 2021). Our analysis identifies a region with a lower rupture velocity (~1.0–1.5 km/s), approximately 33 % to

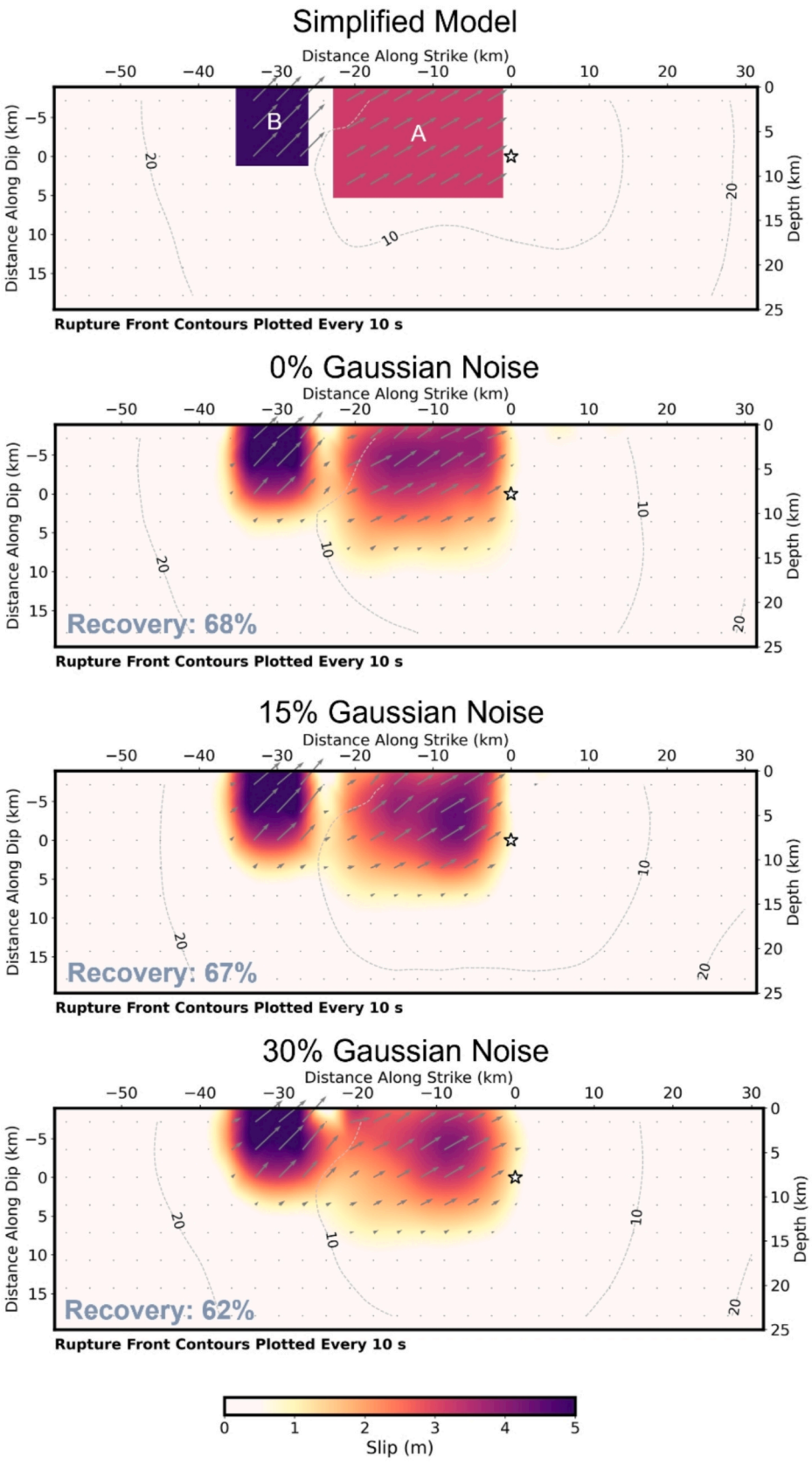

Fig. 11. Synthetic resolution tests for the Chishang earthquake, identical to Fig. 10 but for the Chishang earthquake.

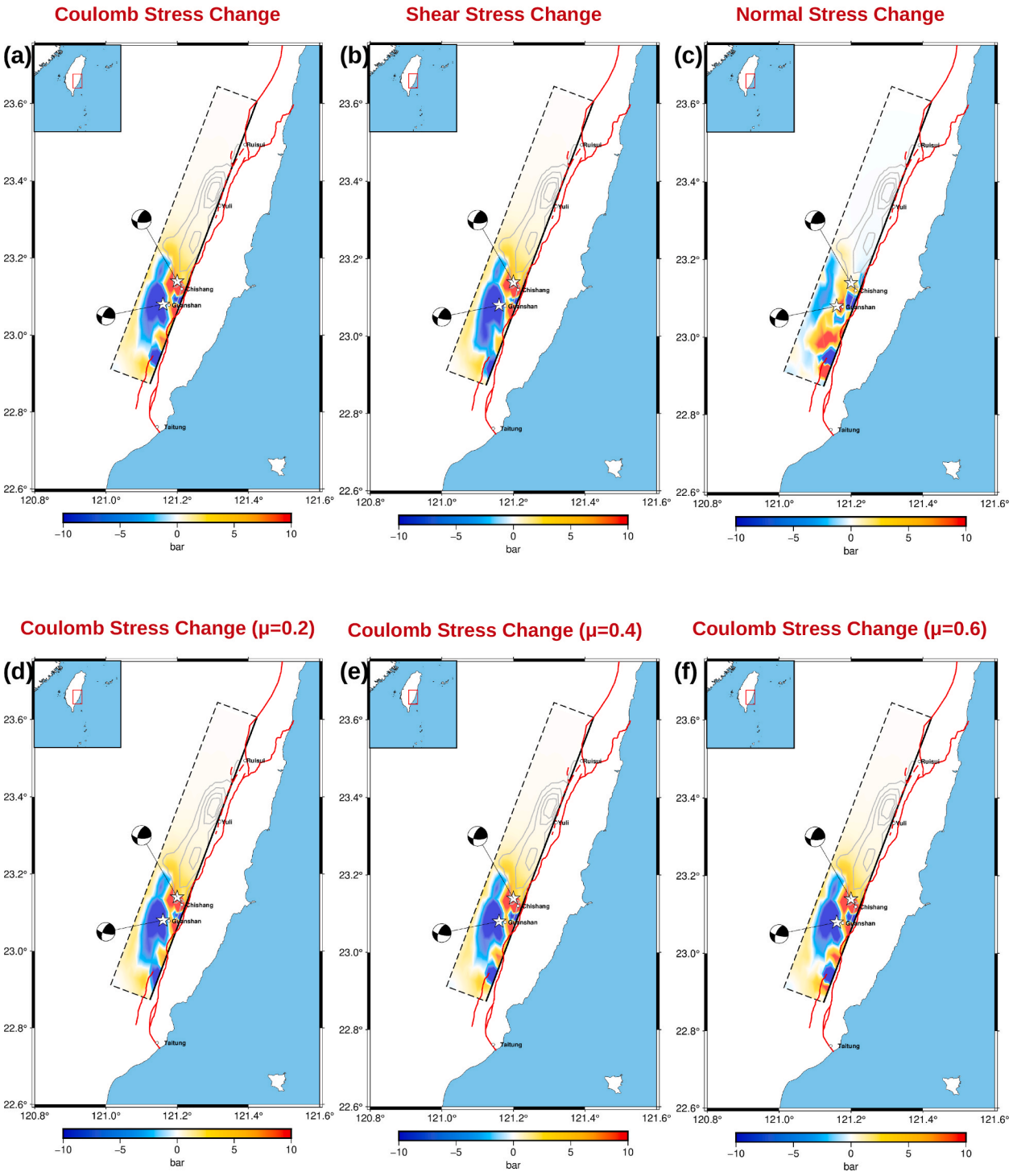

Fig. 12. Stress changes induced on the Chishang earthquake fault plane by the Guanshan earthquake: (a) Coulomb stress change, (b) shear stress change, and (c) normal stress change. Gray contour lines indicate the slip distribution of the Chishang earthquake at 1-m intervals. (d)–(f) show Coulomb stress changes for friction coefficients μ = 0.2, 0.4, and 0.6, respectively. Gray contour lines indicate the slip distribution of the Chishang earthquake at 1-m intervals.

50 % of the S-wave velocity in the source region, located between the two earthquakes (Fig. 13). This low-rupture-velocity region corresponds to the inferred barrier, providing a plausible explanation for the dynamic decoupling of these two events.

While the aftershocks are distributed across the fault plane, the clustering of events near the barrier region (Fig. 14) supports the hypothesis that the barrier influenced fault dynamics by restricting rupture propagation and controlling seismic activity (Madarieta-Txurruka et al., 2022; Xu et al., 2016; Weng et al., 2015). The observed clustering corresponds to a low-slip zone (Fig. 14), which aligns with the low rupture velocity (Fig. 13). Based on previous studies on fault-barrier behavior (Klinger et al., 2006; Madarieta-Txurruka et al., 2022; Xu et al., 2016), we suggest that this low-slip zone reflects fault heterogeneities or barriers that dissipate energy and localize stress accumulation. As the rupture front of the Guanshan earthquake approached this region, the concentrated shear stress at its tip was insufficient to overcome the barrier's resistance, halting forward propagation. Over time, stress accumulated near the barrier, increasing Coulomb stress (Fig. 12),

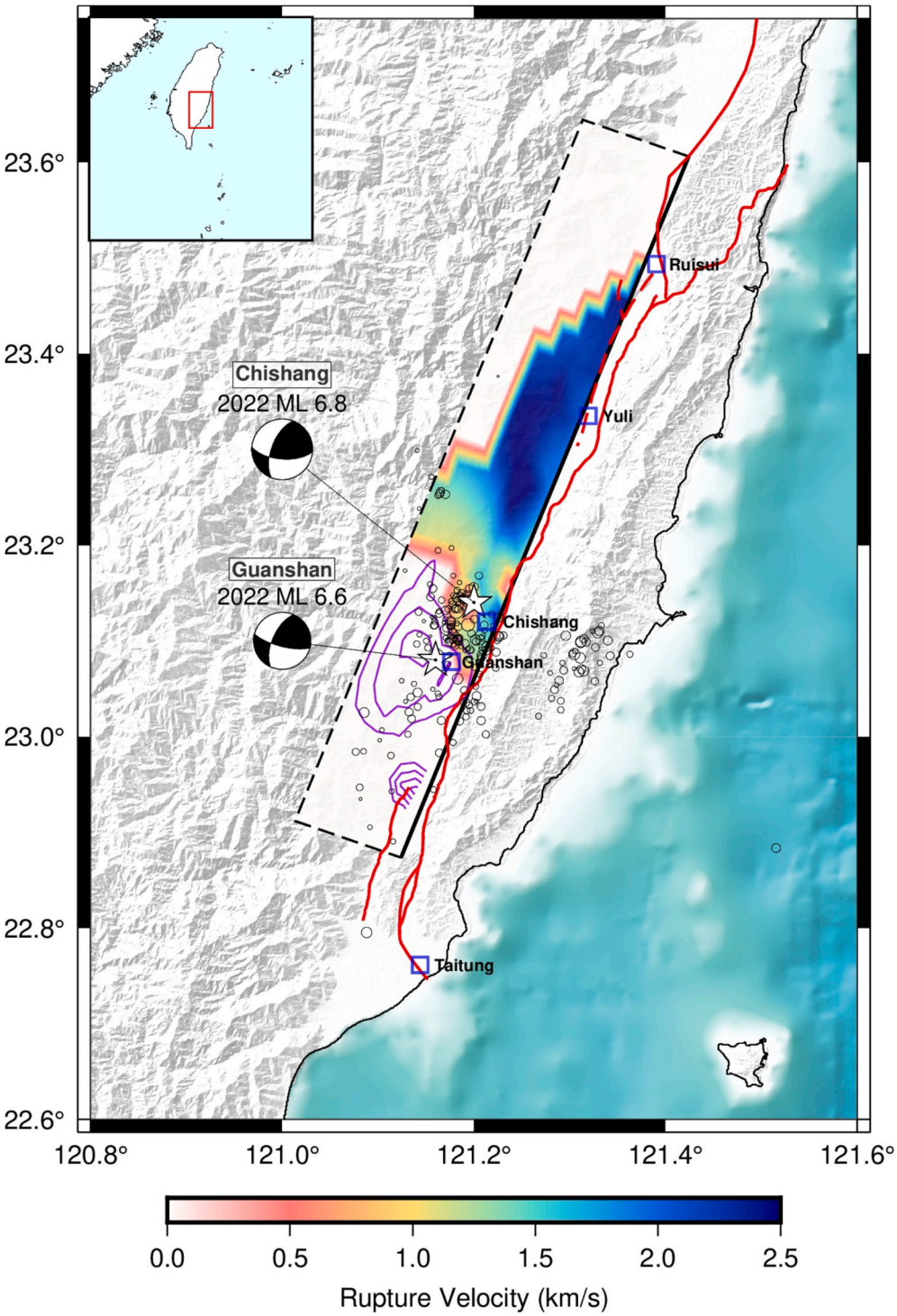

Fig. 13. Rupture velocity distribution on the Chishang earthquake fault plane. White dots mark seismic events that occurred after the Guanshan earthquake but before the Chishang earthquake. Purple contour lines indicate the slip distribution of the Chishang earthquake at 40-cm intervals. (For interpretation of the references to colour in this figure legend, the reader is referred to the web version of this article.)

which likely triggered the nucleation of the Chishang earthquake. This sequence highlights the barrier's role in halting the northward rupture propagation of the Guanshan earthquake, constraining the aftershock distribution, and facilitating stress accumulation that eventually triggered the Chishang earthquake.

Although our interpretation suggests the presence of a physical barrier, alternative explanations may also be possible. For example, Liu et al. (2019) demonstrated that apparent rupture slowdowns may occur at geometrically complex regions of the fault system, such as bends, steps, or segment junctions, where rupture paths become discontinuous or require changes in propagation direction. These geometric complexities can introduce local impedance to rupture propagation as observed in the 2019 Ridgecrest earthquake sequence. In that case, low rupture velocities and high aftershock productivity were attributed to rupture over an immature, segmented fault system. Such geometric effects may similarly influence rupture propagation in our study area. However, Further dynamic analyses are essential to validate these interpretations and improve our understanding of the mechanisms

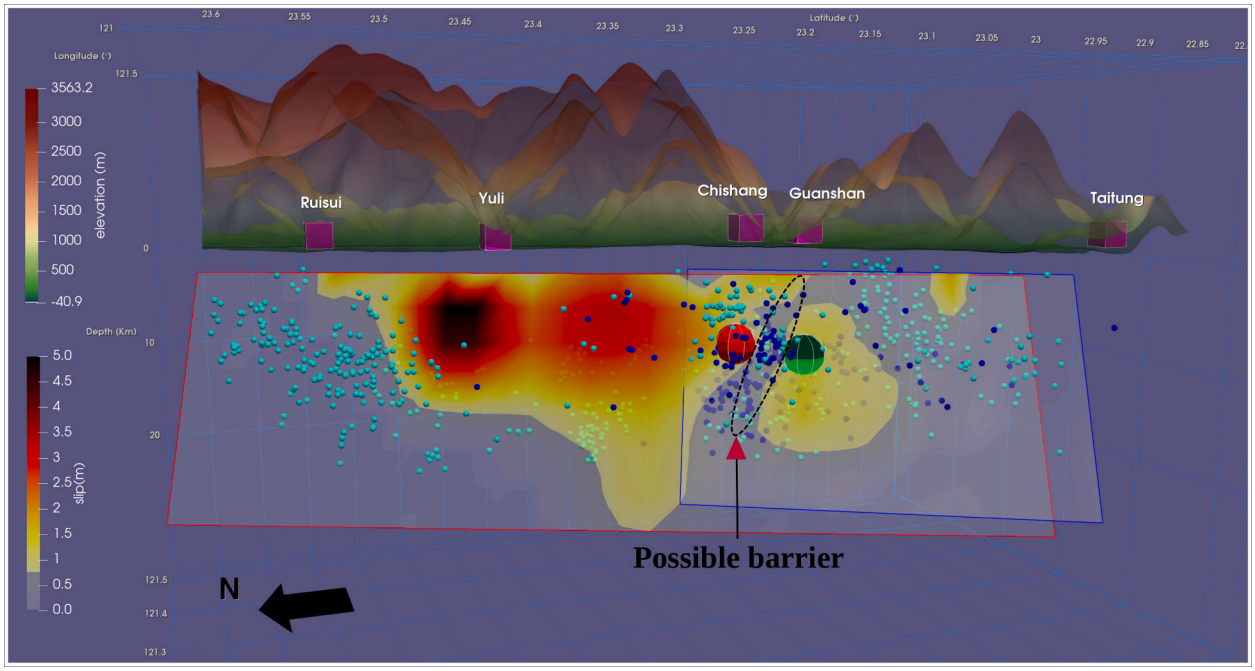

Fig. 14. 3D visualization of the slip distribution and seismicity associated with the Guanshan and Chishang earthquakes. Large green and red dots denote the hypocenters of the Guanshan and Chishang earthquakes, respectively. Smaller blue dots indicate seismicity prior to the Chishang earthquake, while cyan dots represent events afterward. The yellow-to-red–black color scale illustrates the slip distribution on the fault plane, with blue and red outlines marking fault planes of the Guanshan and Chishang earthquakes, respectively. The dashed ellipse highlights the low-slip region between the two hypocenters, consistent with the inferred barrier that likely impeded northward propagation of the Guanshan rupture and contributed to nucleation of the Chishang earthquake. (For interpretation of the references to colour in this figure legend, the reader is referred to the web version of this article.)

underlying this sequence of events.

5. Conclusion

In this study, joint inversions of teleseismic, strong-motion, and GNSS observations delineate source kinematics for the 2022 Guanshan and Chishang earthquakes on the west-dipping Central Range Fault. The key findings are summarized as follows:

(1) The multi-dataset inversion refines rupture imaging, providing tighter constraints on the spatiotemporal slip distribution and rupture kinematics than teleseismic-only solutions, reducing trade-offs between subfault location and rupture timing.
(2) Guanshan ruptured predominantly down-dip and southward with two asperities and a triangular moment-rate function, consistent with left-lateral–reverse kinematics.
(3) The Chishang rupture propagated northward with two shallow asperities, a multi-peaked moment-rate function, and peak slip of ~ 5 m; rupture velocity started low (~1.0–1.5 km/s) and subsequently increased as slip localized on the main patches.
(4) Coulomb stress modeling suggests that stress transferred by the Guanshan rupture favored failure in the Chishang hypocentral region.
(5) A low-velocity barrier inferred between the hypocenters likely limited northward propagation of the Guanshan rupture, which was consistent with the observed aftershock clustering along its margins, and concentrated stress that conditioned the subsequent nucleation of Chishang.

CRediT authorship contribution statement

Wei-Yu Zhang: Writing – original draft, Visualization, Software, Methodology, Investigation, Formal analysis, Data curation, Conceptualization. **Yu-Sheng Sun:** Writing – review & editing, Visualization, Validation, Methodology, Investigation, Formal analysis, Data curation. **Yopi Serhalawan:** Writing – review & editing, Visualization, Software, Project administration, Methodology, Investigation, Formal analysis, Data curation. **Po-Fei Chen:** Writing – review & editing, Validation, Supervision, Resources, Project administration, Methodology, Investigation, Funding acquisition, Formal analysis, Conceptualization. **Ming-Che Hsieh:** Software, Resources, Methodology, Data curation. **Wu-Lung Chang:** Software, Resources, Methodology, Data curation.

Declaration of competing interest

The authors declare that they have no known competing financial interests or personal relationships that could have appeared to influence the work reported in this paper.

Acknowledgments

This work was supported by the Taiwan Earthquake Research Center (TEC), funded through the National Science and Technology Council (NSTC) of Taiwan with Grant Number 114-2923-M-008-002. The TEC Contribution Number for this article is 00207. Additional support was provided by the Industrial Technology Research Institute in Taiwan under Grant Number 202555F0006. Global broadband teleseismic waveform data were retrieved from the NSF SAGE data archive operated by the EarthScope Consortium. Strong-motion data were obtained from the Geophysical Database Management System (GDMS), developed by the Central Weather Administration (CWA) of Taiwan. Some figures were prepared using the Generic Mapping Tools (GMT) version 6 (Wessel et al., 2019) and ParaView (Ayachit, 2015). We thank the editor and the anonymous reviewers for their constructive comments and suggestions, which helped improve the manuscript.

Appendix A. Supplementary data

Supplementary data to this article can be found online at https://doi.org/10.1016/j.jseaes.2025.106940.

Data availability

Data will be made available on request.

References

Ayachit, U., 2015, The ParaView Guide: a parallel Visualization application.

Bock, Y., Melgar, D., Crowell, B.W., 2011. Real-time strong-motion broadband displacements from collocated GPS and accelerometers, 6. Bull. Seismol. Soc. Am. 101 (6), 2904–2925. https://doi.org/10.1785/0120110007.

Central Weather Administration, 2012. Central Weather Administration Seismographic Network [Data set]. International Federation of Digital Seismograph Networks. https://doi.org/10.7914/SN/T5.

Chen, Y., Shin, T., 1998. Study on the earthquake location of 3-D velocity structure in the Taiwan area. Meteorol, Bull 42, 135–169.

Chen, K.H., Toda, S., Rau, R.-J., 2008. A leaping, triggered sequence along a segmented fault: the 1951 ML 7.3 Hualien-Taitung earthquake sequence in eastern Taiwan. J. Geophys. Res. Solid Earth 113, no. B2. https://doi.org/10.1029/2007JB005048.

Cheng, S.-N., Yeh, Y.-T., Yu, M.-S., 1996. The 1951 Taitung earthquake in Taiwan. J.-Geol. Soc. China-Taiwan- 39, 267–286.

Chien, M., Y. Serhalawan, P.-F. Chen, W.-L. Chen, and H.-Y. Kuo, 2025, Spatiotemporal patterns of the 2 April 2024 Hualien earthquake sequence and finite-fault solutions of significant aftershocks, Bull. Seismol. Soc. Am., XX, 1–16, doi: 10.1785/0120250117.

Ching, K.-E., Rau, R.-J., Zeng, Y., 2007. Coseismic source model of the 2003 Mw 6.8 Chengkung earthquake, Taiwan, determined from GPS measurements. J. Geophys. Res. Solid Earth 112 (B6). https://doi.org/10.1029/2006JB004439.

Chuang, R.Y., Johnson, K.M., Kuo, Y.-T., Wu, Y.-M., Chang, C.-H., Kuo, L.-C., 2014. Active back thrust in the eastern Taiwan suture revealed by the 2013 Rueisuei earthquake: evidence for a doubly vergent orogenic wedge? Geophys. Res. Lett. 41 (10), 3464–3470. https://doi.org/10.1002/2014GL060097.

Convertito, V., Pino, N.A., Piccinini, D., 2021. Concentrated slip and low rupture velocity for the May 20, 2012, MW 5.8, Po Plain (Northern Italy) Earthquake Revealed from the Analysis of Source Time Functions. J. Geophys. Res. Solid Earth 126 (1), e2019JB019154. https://doi.org/10.1029/2019JB019154.

Das, S., Henry, C., 2003. Spatial relation between main earthquake slip and its aftershock distribution. Rev. Geophys. 41 (3). https://doi.org/10.1029/2002RG000119.

Ekström, G., Nettles, M., Dziewoński, A.M., 2012. The global CMT project 2004–2010: Centroid-moment tensors for 13,017 earthquakes. Phys. Earth Planet. In. 200–201, 1–9. https://doi.org/10.1016/j.pepi.2012.04.002.

Freed, A.M., 2005. Earthquake triggering by static, dynamic, and postseismic stress transfer. Annu. Rev. Earth Planet. Sci. 33 (33), 335–367. https://doi.org/10.1146/annurev.earth.33.092203.122505.

Goldberg, D.E., Koch, P., Melgar, D., Riquelme, S., Yeck, W.L., 2022. Beyond the teleseism: introducing regional seismic and geodetic data into routine USGS finite-fault modeling, 6. Seismol. Res. Lett. 93 (6), 3308–3323. https://doi.org/10.1785/0220220047.

Goldberg, D. E., D. Melgar, V. J. Sahakian, A. M. Thomas, X. Xu, B. W. Crowell, and J. Geng, 2020, Complex Rupture of an Immature Fault Zone: A Simultaneous Kinematic Model of the 2019 Ridgecrest, CA Earthquakes, 3, Geophys. Res. Lett., 47, no. 3, e2019GL086382, doi: 10.1029/2019GL086382.

Hartzell, S.H., Heaton, T.H., 1983. Inversion of strong ground motion and teleseismic waveform data for the fault rupture history of the 1979 Imperial Valley, California, earthquake. Bull. Seismol. Soc. Am. 73 (6A), 1553–1583. https://doi.org/10.1785/BSSA07306A1553.

Heaton, T.H., 1990. Evidence for and implications of self-healing pulses of slip in earthquake rupture, 1. Phys. Earth Planet. In. 64 (1), 1–20. https://doi.org/10.1016/0031-9201(90)90002-F.

Ji, C., Wald, D.J., Helmberger, D.V., 2002. Source description of the 1999 hector mine, california, earthquake, Part I: wavelet domain inversion theory and resolution analysis, 4. Bull. Seismol. Soc. Am. 92 (4), 1192–1207. https://doi.org/10.1785/0120000916.

Kao, H., Shen, S.J., Ma, K., 1998. Transition from oblique subduction to collision: Earthquakes in the southernmost Ryukyu arc-Taiwan region. J. Geophys. Res. Atmos. 103 (B4), 7211–7229. https://doi.org/10.1029/97jb03510.

King, G.C.P., Stein, R.S., Lin, J., 1994. Static stress changes and the triggering of earthquakes. Bull. Seismol. Soc. Am. 84 (3), 935–953. https://doi.org/10.1785/BSSA0840030935.

Koch, P., Bravo, F., Riquelme, S., Crempien, J.G.F., 2019. Near-real-time finite-fault inversions for large earthquakes in Chile using strong-motion data, 5. Seismol. Res. Lett. 90 (5), 1971–1986. https://doi.org/10.1785/0220180294.

Kuochen, H., Wu, Y.-M., Chang, C.-H., Hu, J.-C., Chen, W.-S., 2004. Relocation of eastern Taiwan earthquakes and tectonic implications. Terr. Atmospheric Ocean. Sci. 15 (4), 647. https://doi.org/10.3319/tao.2004.15.4.647.

Kuochen, H., Wu, Y.-M., Chen, Y.-G., Chen, R.-Y., 2007. 2003 Mw6.8 Chengkung earthquake and its related seismogenic structures. J. Asian Earth Sci. 31 (3), 332–339. https://doi.org/10.1016/j.jseaes.2006.07.028.

Lee, J.-C., Angelier, J., Chu, H.-T., Hu, J.-C., Jeng, F.-S., 2001. Continuous monitoring of an active fault in a plate suture zone: a creepmeter study of the Chihshang Fault, eastern Taiwan. Tectonophysics 333 (1), 219–240. https://doi.org/10.1016/S0040-1951(00)00276-6.

Lee, J.-C., Angelier, J., Chu, H.-T., Hu, J.-C., Jeng, F.-S., Rau, R.-J., 2003. Active fault creep variations at Chihshang, Taiwan, revealed by creep meter monitoring, 1998–2001. J. Geophys. Res. Solid Earth 108 (B11). https://doi.org/10.1029/2003JB002394.

Lee, S.-J., Huang, H.-H., Shyu, J.B.H., Yeh, T.-Y., Lin, T.-C., 2014. Numerical earthquake model of the 31 October 2013 Ruisui, Taiwan, earthquake: source rupture process and seismic wave propagation. J. Asian Earth Sci. 96, 374–385. https://doi.org/10.1016/j.jseaes.2014.09.020.

Lee, S.-J., Liu, T.-Y., Lin, T.-C., 2023. The role of the west-dipping collision boundary fault in the Taiwan 2022 Chihshang earthquake sequence. Sci. Rep. 13 (1), 3552. https://doi.org/10.1038/s41598-023-30361-0.

Lee, S.-J., Ma, K.-F., Chen, H.-W., 2006. Effects of fault geometry and slip style on near-fault static displacements caused by the 1999 Chi-Chi, Taiwan earthquake. Earth Planet. Sci. Lett. 241 (1), 336–350. https://doi.org/10.1016/j.epsl.2005.09.064.

Li, B., Li, Y., Jiang, W., Su, Z., Shen, W., 2020. Conjugate ruptures and seismotectonic implications of the 2019 Mindanao earthquake sequence inferred from Sentinel-1 InSAR data. Int. J. Appl. Earth Obs. Geoinformation 90, 102127. https://doi.org/10.1016/j.jag.2020.102127.

Liu, C., Lay, T., Brodsky, E.E., Dascher-Cousineau, K., Xiong, X., 2019. Coseismic rupture process of the large 2019 ridgecrest earthquakes from joint inversion of geodetic and seismological observations. Geophys. Res. Lett. 46 (21), 11820–11829. https://doi.org/10.1029/2019GL084949.

Liu, K.-S., Shin, T.-C., Tsai, Y.-B., 1999. A Free-Field strong motion network in Taiwan: TSMIP. Terr. Atmos. Ocean. Sci. 10 (2), 377. https://doi.org/10.3319/tao.1999.10.2.377(t).

Madarieta-Txurruka, A., González-Castillo, L., Peláez, J.A., Catalán, M., Henares, J., Gil, A.J., Lamas-Fernández, F., Galindo-Zaldívar, J., 2022. The role of faults as barriers in Confined seismic sequences: 2021 Seismicity in the Granada Basin (Betic Cordillera). Tectonics 41, no. 9. https://doi.org/10.1029/2022tc007481.

Melgar, D., Crowell, B.W., Melbourne, T.I., Szeliga, W., Santillan, M., Scrivner, C., 2020. Noise Characteristics of Operational Real-Time High-Rate GNSS Positions in a Large Aperture Network, 7. J. Geophys. Res. Solid Earth 125, no. 7, e2019JB019197. https://doi.org/10.1029/2019JB019197.

Materna, K., 2023, Elastic_stresses_py (version 1.0.0). https://github.com/kmaterna/Elastic_stresses_py. Archived at doi: 10.5281/zenodo.79751979.

Melgar, D., Ganas, A., Geng, J., Liang, C., Fielding, E.J., Kassaras, I., 2017. Source characteristics of the 2015 Mw6.5 Lefkada, Greece, strike-slip earthquake, 3. J. Geophys. Res. Solid Earth 122 (3), 2260–2273. https://doi.org/10.1002/2016JB013452.

Okada, Y., 1985. Surface deformation due to shear and tensile faults in a half-space, 4. Bull. Seismol. Soc. Am. 75 (4), 1135–1154. https://doi.org/10.1785/BSSA0750041135.

Shao, G., Li, X., Ji, C., Maeda, T., 2011. Focal mechanism and slip history of the 2011 Mw 9.1 off the Pacific coast of Tohoku Earthquake, constrained with teleseismic body and surface waves, 7. Earth Planets Space 63, no. 7, 9. https://doi.org/10.5047/eps.2011.06.028.

Shyu, J.B.H., Sieh, K., Chen, Y.-G., Liu, C.-S., 2005a. Neotectonic architecture of Taiwan and its implications for future large earthquakes. J. Geophys. Res. Solid Earth 110, no. B8. https://doi.org/10.1029/2004JB003251.

Shyu, J.B.H., Sieh, K., Chen, Y.-G., 2005b. Tandem suturing and disarticulation of the Taiwan orogen revealed by its neotectonic elements. Earth Planet. Sci. Lett. 233 (1), 167–177. https://doi.org/10.1016/j.epsl.2005.01.018.

Shyu, J.B.H., Sieh, K., Chen, Y.-G., Chung, L.-H., 2006a. Geomorphic analysis of the Central Range fault, the second major active structure of the Longitudinal Valley suture, eastern Taiwan. GSA Bull. 118 (11–12), 1447–1462. https://doi.org/10.1130/B25905.1.

Shyu, J.B.H., Sieh, K., Avouac, J.-P., Chen, W.-S., Chen, Y.-G., 2006b. Millennial slip rate of the Longitudinal Valley fault from river terraces: Implications for convergence across the active suture of eastern Taiwan. J. Geophys. Res. Solid Earth 111 (B8). https://doi.org/10.1029/2005JB003971.

Sun, Y.-S., et al., 2024. The 2020 Mw 7.0 Samos (Eastern Aegean Sea) Earthquake: joint source inversion of multitype data, and tsunami modelling. Geophys. J. Int. 237 (3), 1285–1300. https://doi.org/10.1093/gji/ggae082.

Wald, D.J., Heaton, T.H., 1994. Spatial and temporal distribution of slip for the 1992 Landers, California, earthquake. Bull. Seismol. Soc. Am. 84 (3), 668–691. https://doi.org/10.1785/BSSA0840030668.

Wald, D.J., Heaton, T.H., Hudnut, K.W., 1996. The slip history of the 1994 Northridge, California, earthquake determined from strong-motion, teleseismic, GPS, and leveling data. Bull. Seismol. Soc. Am. 86 (1B), S49–S70. https://doi.org/10.1785/BSSA08601B0S49.

Wang, K., Dreger, D.S., Tinti, E., Bürgmann, R., Taira, T., 2020. Rupture process of the 2019 ridgecrest, California Mw 6.4 Foreshock and Mw 7.1 earthquake constrained by seismic and geodetic data. Bull. Seismol. Soc. Am. 110 (4), 1603–1626. https://doi.org/10.1785/0120200108.

Wang, R., Schurr, B., Milkereit, C., Shao, Z., Jin, M., 2011. An improved automatic scheme for empirical baseline correction of digital strong-motion records. Bull. Seismol. Soc. Am. 101 (5), 2029–2044. https://doi.org/10.1785/0120110039.

Weng, H., Huang, J., Yang, H., 2015. Barrier-induced supershear ruptures on a slip-weakening fault. Geophys. Res. Lett. 42 (12), 4824–4832. https://doi.org/10.1002/2015gl064281.

Wessel, P., Luis, J.F., Uieda, L., Scharroo, R., Wobbe, F., Smith, W.H.F., Tian, D., 2019. The generic mapping tools version 6. Geochem. Geophys. Geosyst. 20 (11), 5556–5564. https://doi.org/10.1029/2019gc008515.

Wetzler, N., Lay, T., Brodsky, E.E., Kanamori, H., 2018. Systematic deficiency of aftershocks in areas of high coseismic slip for large subduction zone earthquakes. Sci. Adv. 4, no. 2, eaao3225. https://doi.org/10.1126/sciadv.aao3225.

Wu, Y.-M., Chen, Y.-G., Chang, C.-H., Chung, L.-H., Teng, T.-L., Wu, F.T., Wu, C.-F., 2006. Seismogenic structure in a tectonic suture zone: with new constraints from 2006 Mw6.1 Taitung earthquake. Geophys. Res. Lett. 33, no. 22. https://doi.org/10.1029/2006GL027572.

Xu, J., Zhang, Z., Chen, X., 2016. The effects of barriers on supershear rupture. Geophys. Res. Lett. 43 (14), 7478–7485. https://doi.org/10.1002/2016gl069701.

Yan, Z., X. Xiong, C. Liu, and J. Xu, 2022, Integrated Analysis of the 2020 Mw 7.4 La Crucecita, Oaxaca, Mexico, Earthquake from Joint Inversion of Geodetic and Seismic Observations, Bull. Seismol. Soc. Am., 112, no. 3, 1271–1283, doi: 10.1785/0120210276.

Yao, Z.X., Ji, 1997. Finite fault inversion in the time domain. Chin. J. Geophys. 40.

Yu, S.-B., Chen, H.-Y., Kuo, L.-C., 1997. Velocity field of GPS stations in the Taiwan area. Tectonophysics 274 (1), 41–59. https://doi.org/10.1016/S0040-1951(96)00297-1.

Yu, S.-B., Kuo, L.-C., 2001. Present-day crustal motion along the Longitudinal Valley Fault, eastern Taiwan. Tectonophysics 333 (1), 199–217. https://doi.org/10.1016/S0040-1951(00)00275-4.

Yu, S.B., Liu, C.C., 1989. Fault creep of the central segment of the Longitudinal Valley Fault, Eastern Taiwan, Fault Creep Cent. Segm. Longitudinal Val. Fault East. Taiwan 32 (3), 209–231.

Yuan, J., Wang, J., Zhu, S., 2020. Effects of barriers on fault rupture process and strong ground motion based on various friction laws, 5. Appl. Sci. 10 (5), 1687. https://doi.org/10.3390/app10051687.

Zhou, X., Xie, Y., Bi, J., Berto, F., 2019. Numerical simulation of supershear ruptures in rock mass based on general particle dynamics. Fatigue Fract. Eng. Mater. Struct. 42 (4), 905–918. https://doi.org/10.1111/ffe.12959.

Zhu, L., Rivera, L.A., 2002. A note on the dynamic and static displacements from a point source in multilayered media, 3. Geophys. J. Int. 148 (3), 619–627. https://doi.org/10.1046/j.1365-246X.2002.01610.x.